Analysis of melting by natural convection in an enclosure

Adrian Bejan
Department of Mechanical Engineering and Materials Science, Duke University, Durham, NC, USA

This paper reports theoretical solutions for the quasi-steady and time-dependent regimes of melting in the presence of natural convection in an enclosed phase-change material heated from the side. The first part consists of developing two boundary layer solutions for the flows near the heated wall and the solid–liquid interface, and then matching these solutions with a unique solution for the core of the liquid region. The second part of the paper outlines an analysis for the earlier, time-dependent regime, when the liquid counterflow through the slender gap convects heat in the vertical direction. This two-part analysis shows that the liquid superheat (Stefan number, Ste) has a sizeable effect on the flow and temperature fields. As Ste increases, the average melting rate decreases and the overall heat transfer rate into the enclosure increases.

Keywords: phase change; natural convection; enclosures

Background

There are few "compact" problems in modern heat transfer that have attracted as much attention as the problem of melting in the presence of natural convection in an enclosure heated from the side. A segment of the literature devoted to this problem has been reviewed by Viskanta.[1] My own interest in it was sparked by the discrepancy between the large volume of this literature and the absence of a purely theoretical description of the phenomenon. A first analytical step for me in this field was the scale analysis, that is, the work of identifying the proper scales of the phenomenon, in order to construct scaling-correct correlations for the heat transfer and melting rates.[2] The objective of the present paper is to demonstrate that it is possible to go significantly beyond scale analysis and to produce an entirely theoretical description of the heat transfer and melting process.

The most important feature of the analysis described in this paper is that it accounts for the lateral movement of the two-phase interface. Starting with Figure 1, the analysis focuses on the slender (boundary layer) flow near the interface, for which the frame x-y is attached to the interface and migrates slowly to the left. The two-phase interface undergoes a deformation as it migrates to the left (i.e., the y axis becomes curved), because the melting rate increases with altitude (e.g., Figure 4). However, since the flow region is assumed to remain boundary-layer-like throughout the time interval for which the analysis is valid, it has been drawn straight and vertical in Figure 1.

The flow region near the heated wall of the enclosure is assumed to be slender as well. This flow is studied in the frame x_r-y, which is stationary and attached to the right wall in Figure 1. By taking into account the movement of the melting front away from the heated wall, it is possible to show how the liquid phase superheat (the Stefan number) affects the overall heat transfer and melting rates.

The analysis is based on a number of classical simplifying assumptions. The heated wall is maintained at constant temperature. The solid portion of the phase-change material is isothermal and at the melting point. The densities of the solid and liquid phases are equal, and the liquid is assumed to be Newtonian and Boussinesq incompressible.

Cold boundary layer

The analysis of the convection dominated (quasi-steady) regime consists of developing two boundary layer solutions, one for the cold interface and the other for the heated wall, and then meshing these solutions to a unique solution for the core region. The method is the same as the one employed by Gill[3] in the pure natural convection problem. The new feature contributed by the present analysis is the effect of melting along the solid–liquid interface, i.e., along the cold side of the cavity filled with liquid.

In the system of coordinates x-y attached to the solid–liquid interface, the boundary layer equations for the conservation of momentum and energy are (see, for example, Ref. 4, pp. 112, 114)

$$u\frac{\partial v}{\partial x}+v\frac{\partial v}{\partial y}=\nu\frac{\partial^2 v}{\partial x^2}+g\beta(T-T_c) \tag{1}$$

$$u\frac{\partial T}{\partial x}+v\frac{\partial T}{\partial y}=\alpha\frac{\partial^2 T}{\partial x^2} \tag{2}$$

The symbols appearing in these and subsequent equations are defined in Figure 1 and the Notation. Worth noting is that x and y are assigned, respectively, to the horizontal and vertical directions, in accordance to the boundary layer natural convection treatment of Ref. 4.

In the analysis that is presented below, the inertia terms appearing on the left side of the momentum equation (1) will be neglected. The neglect of these terms is justified not only at $x=0$ but over the entire thickness of the thermal boundary layer (δ in Figure 1), provided the Prandtl number of the liquid is greater than 1. Inside the thermal boundary layer region, the

Address reprint requests to Dr. Bejan at the Department of Mechanical Engineering and Materials Science, Duke University, Durham, NC 27706, USA.

Received 21 April 1988; accepted 17 January 1989

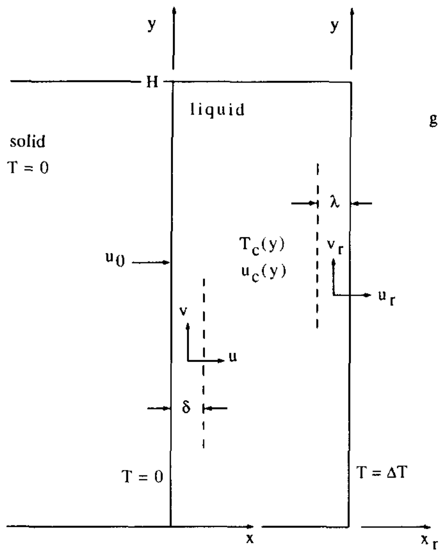

Figure 1 Enclosed phase-change material heated from the side

momentum balance is between the driving effect of buoyancy and the retardant effect of viscous shear. The analytical proof of these statements can be found in Kuiken,[5] Patterson and Imberger,[6] and on pp. 114–118 of Ref. 4.

The first step in the analysis is to assume the shape of the temperature and velocity profiles across the cold boundary layer (thickness δ) and to solve the integral versions of Equations 1 and 2. In Gill's original Oseen-linearized analysis the assumed profile shapes had exponential decays near the vertical surface. More recently, Blythe and Simpkins[7] have shown that considerably better agreement is achieved between the heat transfer result of this type of analysis and numerical experiments if the assumed profiles are described by polynomials. The value of their discovery is stressed further by the integral analysis of the classical vertical plate problem (Ref. 4, pp. 122–125), which showed that in the $\mathrm{Pr} \gg 1$ range the use of Squire's polynomial profiles[8] is clearly superior to the use of exponential profiles.

For this reason, we assume Squire-type profiles for both the temperature and vertical velocity distributions in the thermal boundary layer $0 \le x \le \delta$,

$$T = T_c \frac{x}{\delta}\left(2 - \frac{x}{\delta}\right) \tag{3}$$

$$v = V \frac{x}{\delta}\left(1 - \frac{x}{\delta}\right)^2 \tag{4}$$

in which $T_c(y)$ is the temperature distribution (thermal stratification) of the core region. The unknown function $V(y)$ follows from the momentum equation (1), which for the thermal boundary layer region of a "$\mathrm{Pr} > 1$" liquid reduces to

$$\frac{\partial^2 v}{\partial x^2} = \frac{g\beta}{\nu}(T_c - T) \tag{5}$$

Next, we force the profiles 3 and 4 to satisfy the equation obtained by integrating Equation 5 from $x = 0$ to $x = \delta$. The result of this operation is

$$V = -\frac{g\beta}{3\nu} T_c \delta^2 \tag{6}$$

Turning now our attention to the energy equation, we force the same profiles to satisfy the $\int_0^\delta (\ )\,\mathrm{d}x$ integral of Equation 2, which reads

$$u_\delta T_\delta - u_0 T_0 + \frac{\mathrm{d}}{\mathrm{d}y}\int_0^\delta vT\,\mathrm{d}x = \alpha \left.\frac{\partial T}{\partial x}\right|_0^\delta \tag{7}$$

Note first that $T_\delta = T_c$. The solid–liquid interface temperature

Notation

B	Function, Equation 41
c	Specific heat of liquid
C	Constant, Equation 23
C_1	Constant, Equation 37
g	Gravitational acceleration
G	Function, Equation 55
G_c	Function, Equation 47
G_r	Function, Equation 50
h_{sf}	Latent heat of fusion
H	Height
k	Thermal conductivity of liquid
Nu	Overall Nusselt number for the solid–liquid interface, Equation 31
Nu_r	Overall Nusselt number for the heated side, Equation 29
Q	Total heat transfer rate through the solid–liquid interface
Q_c	Convection heat transfer rate, Equation 45
Q_r	Total heat transfer rate through the heated wall
Ra	Rayleigh number, Equation 13
Ste	Stefan number, Equation 14
t	Time
T	Excess temperature above the melting point
$\tilde{T}$	Dimensionless temperature, Equation 36
ΔT	Temperature difference between the right wall and the interface

T_c	Core temperature
u, v	Velocity components, Figure 1 (see also u_r, v_r)
u_0	Melting velocity, Equations 10, 24
$\bar{u}_0$	Average melting velocity, Equation 25
$\tilde{v}$	Dimensionless vertical velocity, Equation 38
V	Function, Equation 6
x, y	System of coordinates, Figure 1 (see also x_r, y)
x_1	Horizontal coordinate, Figure 6
X	Liquid gap thickness, Figure 6
$\tilde{y}$	Dimensionless vertical position, Equation 12
α	Thermal diffusivity of liquid
β	Coefficient of thermal expansion
δ	Thickness of cold boundary layer
$\tilde{\delta}$	Dimensionless cold boundary layer thickness, Equation 12
θ	Dimensionless time, Equation 46
λ	Thickness of warm boundary layer
$\tilde{\lambda}$	Dimensionless warm boundary layer thickness
ξ	Dimensionless horizontal position, Equation 36
ν	Kinematic viscosity of liquid
ρ	Density of liquid, density of solid
τ	Dimensionless core temperature, Equation 12
Φ, Φ_r	Functions of Stefan number, Equations 27, 30, and Figure 5
$(\ )_r$	Pertaining to the right side of the liquid region, Figure 1

is zero because T represents the excess temperature above the melting point of the phase-change material. The entrainment velocity function $u_\delta(y)$ is obtained from the mass conservation equation

$$\frac{\partial u}{\partial x}+\frac{\partial v}{\partial y}=0 \tag{8}$$

which, integrated from $x=0$ to $x=\delta$, yields

$$u_\delta=u_0-\frac{d}{dy}\int_0^\delta v\,dx \tag{9}$$

And, since the x-y system of coordinates is attached to the slowly receding interface, the horizontal velocity through the interface (the "blowing" or "melting" velocity) is directly proportional to the heat flux on the interface:

$$u_0=\frac{k}{\rho h_{sf}}\left(\frac{\partial T}{\partial x}\right)_{x=0} \tag{10}$$

Recall at this point that the solid is isothermal and at $T=0$, i.e., that there is no conduction into the solid. All the heat that is transferred from the boundary layer to the interface is balanced by the latent heat of melting of the newly formed liquid.

The end result of combining Equations 7–10 with the assumed profiles 3 and 4 is the energy-integral equation

$$2\,\mathrm{Ste}\frac{\tau^2}{\tilde{\delta}}+\frac{\tau}{36}\frac{d}{d\tilde{y}}(\tau\tilde{\delta}^3)-\frac{1}{60}\frac{d}{d\tilde{y}}(\tau^2\tilde{\delta}^3)=-2\frac{\tau}{\tilde{\delta}} \tag{11}$$

This dimensionless form is based on the new variables

$$\tilde{y}=\frac{y}{H},\quad \tilde{\delta}=\frac{\delta}{H}\mathrm{Ra}^{1/4},\quad \tau=\frac{T_c}{\Delta T} \tag{12}$$

in which Ra is the Rayleigh number based on the height of the interface and the overall (imposed) temperature difference:

$$\mathrm{Ra}=\frac{g\beta H^3\Delta T}{\alpha\nu} \tag{13}$$

The dimensionless group Ste is the Stefan number for the liquid phase:

$$\mathrm{Ste}=\frac{c\,\Delta T}{h_{sf}} \tag{14}$$

In summary, the integral analysis of the cold boundary layer results in one equation, Equation 11, involving two unknown functions of altitude, $\tau(\tilde{y})$ and $\tilde{\delta}(\tilde{y})$. In order to close the quasi-steady regime problem, we must consider the boundary layer flow along the heated wall.

Warm boundary layer

The temperature of the right wall of the enclosure is being maintained at $T=\Delta T$. The analysis of the warm boundary layer follows the same steps as the analysis of the cold boundary layer, therefore, we shall skip some of the details. With reference to the x_r-y system of coordinates shown in Figure 1, the Squire-type profiles assumed for temperature and vertical velocity are:

$$T_r=(\Delta T-T_c)\left(1+\frac{x_r}{\lambda}\right)^2+T_c \tag{15}$$

$$v_r=-\frac{g\beta}{3\nu}(\Delta T-T_c)\lambda^2\frac{x_r}{\lambda}\left(1+\frac{x_r}{\lambda}\right)^2 \tag{16}$$

where $\lambda(y)$ is the thickness of the warm boundary layer.

Integrating the energy equation across the warm boundary layer we obtain

$$(u_rT_r)_{-\lambda}-(u_rT_r)_0+\frac{d}{dy}\int_0^{-\lambda}v_rT_r\,dx_r=\alpha\left.\frac{\partial T_r}{\partial x_r}\right|_0^{-\lambda} \tag{17}$$

in which $(T_r)_{-\lambda}=T_c$. The entrainment velocity $(u_r)_{-\lambda}$ is again related to the change in the vertical flowrate through the warm layer. This relation is provided by the integral of the mass conservation equation

$$(u_r)_{-\lambda}=(u_r)_0-\frac{d}{dy}\int_0^{-\lambda}v_r\,dx_r \tag{18}$$

In both Equations 17 and 18 we substitute $(u_r)_0=0$ because the right wall is impermeable.

In the end, that is after forcing the profiles (15,16) to satisfy Equation 17, we obtain the energy-integral equation for the right side

$$\frac{1}{90}\frac{d}{d\tilde{y}}[(1-\tau)^2\tilde{\lambda}^3]+\frac{1}{36}(1-\tau)\tilde{\lambda}^3\frac{d\tau}{d\tilde{y}}=2\frac{1-\tau}{\tilde{\lambda}} \tag{19}$$

The dimensionless $\tilde{y}$ and τ appearing in this equation have been defined already in Equation 12; the dimensionless boundary layer thickness $\tilde{\lambda}$ is defined in the same manner as $\tilde{\delta}$

$$\tilde{\lambda}=\frac{\lambda}{H}\mathrm{Ra}^{1/4} \tag{20}$$

Summarizing the results of the two boundary layer analyses, we see two ordinary differential equations, Equations 11 and 19, containing three unknown functions, $\tau(\tilde{y})$, $\tilde{\delta}(\tilde{y})$ and $\tilde{\lambda}(\tilde{y})$. The problem will finally be closed through the act of matching the two boundary layer solutions, which is described next.

Core region

The matching of the two boundary layer solutions is effected by the requirement that the two boundary layers communicate with the same core region. This requirement is met already by the temperature field, as both boundary layer temperatures (T and T_r of Equations 3 and 15) equal the same core temperature T_c at their respective outer edges. The velocity field, however, does not meet this requirement, because the cold-side entrainment velocity u_δ of Equation 9 is not the same as the warm-side value $(u_r)_{-\lambda}$, Equation 18.

Let $u_c(y)$ represent the unique horizontal velocity distribution through the core. It is clear that since the right wall is stationary with respect to the core region, $u_c(y)$ is the same as the warm-side entrainment velocity $(u_r)_{-\lambda}$. On the cold side of the core region we note that the cold boundary layer and the solid–liquid interface to which it is attached migrate toward the left with the melting velocity u_0. Therefore, relative to the cold boundary layer solution of the second section, the true core velocity distribution u_c is equal to the difference $u_\delta-u_0$. The net result of this entire argument is that the cold-side and warm-side entrainment velocities are related by,

$$u_\delta-u_0=(u_r)_{-\lambda} \tag{21}$$

which, after using Equations 9, 18, $(u_r)_0=0$ and the dimensionless notation defined earlier, reads

$$\frac{d}{d\tilde{y}}(\tau\tilde{\delta}^3)=\frac{d}{d\tilde{y}}[(1-\tau)\tilde{\lambda}^3] \tag{22}$$

Equation 22 is the third equation that was needed in order to close the problem summarized at the end of the third section. Integrating Equation 22 once we obtain

$$\tau\tilde{\delta}^3=(1-\tau)\tilde{\lambda}^3+C \tag{23}$$

in which the constant C must be zero so that the warm boundary layer "starts" (i.e., $\tilde\lambda = 0$) from the bottom end of the heated wall ($\tilde y = 0$) where the adjacent core temperature is the lowest ($\tau = 0$). Alternatively, one can argue that C is zero because the cold boundary layer starts ($\tilde\delta = 0$) from its top end ($\tilde y = 1$) where the core temperature is the highest ($\tau = 1$). It is easy to show that the same conclusion ($C = 0$) is reached by arguing, as done originally by Gill[3], that the top and bottom ends of the liquid cavity are impermeable.

Beyond this point, the solution for $\tau(\tilde y)$, $\tilde\delta(\tilde y)$, and $\tilde\lambda(\tilde y)$ was pursued numerically. Equations 11, 19, and 23 (with $C = 0$) were integrated by marching in steps of τ instead of steps of $\tilde y$. The shape of the $\tau(\tilde y)$ function, Figure 2, shows that uniform steps in τ bring about much finer steps in $\tilde y$ near the ends of the two boundary layers ($\tilde y = 0$) and ($\tilde y = 1$), that is, precisely in the regions that contribute the most to the overall heat transfer between the two sides of the liquid region.

The numerical integration of each Ste case started from $\tau = 0$ (i.e., from the bottom) where $\tilde y = 0$ and $\tilde\lambda = 0$. A guess had to be made for the value of one boundary layer thickness at the first τ node, $\tau = \Delta\tau$. The integration continued then all the way up to $\tau = 1$, where the value of the emerging final value of $\tilde y$ was compared with 1. In case of disagreement, the initial guess made for $\tilde\lambda$ (or $\tilde\delta$) at the first τ node was improved. Grid fineness tests showed that a uniform division of the τ domain into 2000 steps was sufficient for guaranteeing better than 1% accuracy in all the calculated quantities, including the overall Nusselt number discussed in the next section.

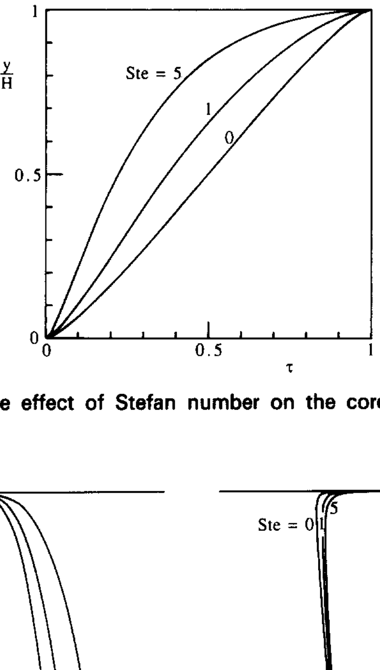

Figure 2 The effect of Stefan number on the core temperature distribution

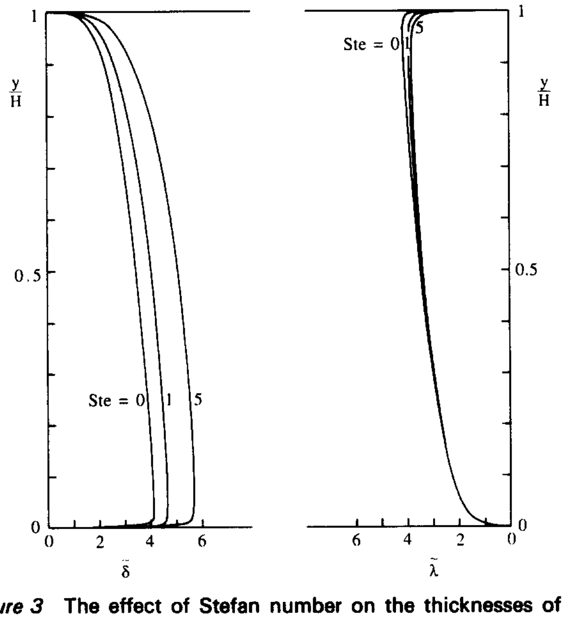

Figure 3 The effect of Stefan number on the thicknesses of the two boundary layers

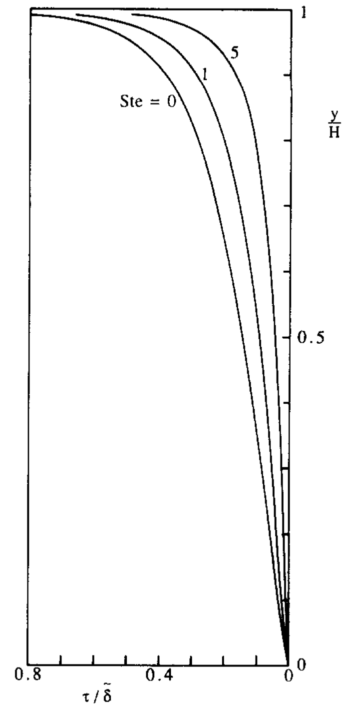

Figure 4 The shape of the solid–liquid interface

Figure 2 shows the temperature distribution in the core region. We see that at any given altitude the core temperature decreases as the Stefan number increases. Put another way, when the Stefan number is finite the average temperature of the core region ($\int_0^1 \tau \, d\tilde y$) is less than 1/2. Worth keeping in mind is that the average core temperature equals 1/2 in the regime dominated by natural convection[3,7], and in the absence of melting.

Figure 3 combines the solutions obtained for the cold-side and warm-side boundary layer thicknesses. Each boundary layer drops sharply to zero thickness at both ends of the liquid cavity. The new feature contributed by this work is the effect of the Stefan number, which is most pronounced on the thickness of the cold boundary layer. The cold boundary layer becomes thicker as the Stefan number increases. At the same time, the warm boundary layer becomes thinner, especially in its upper region. We shall see that this effect translates into lower melting rates and higher heating rates from the right wall, as Ste increases.

The present solution also offers a glimpse of the shape of the nearly vertical solid–liquid interface, which was discussed in the first section. Since in the boundary layer convection regime the heating and melting phenomenon is quasi-steady, at each y value the solid–liquid interface migrates toward the left with the constant speed u_0 of Equation 10. Therefore, at each point in time the shape of the interface has the same y dependence as the u_0 function. Combining Equations 3 and 10, u_0 can be rewritten as

$$u_0 = 2\frac{k\,\Delta T}{\rho h_{sf} H}\mathrm{Ra}^{1/4}\frac{\tau(\tilde y)}{\tilde\delta(\tilde y)} \qquad (24)$$

showing that the shape of the interface is the same as that of the function $\tau/\tilde\delta$. Figure 4 shows this shape and the manner in which it is affected by changes in the Stefan number. The solid–liquid interface becomes relatively straighter over a larger portion of its height as Ste increases.

Quasi-steady heat transfer and melting rates

The two overall quantities of interest in the quasi-steady or boundary layer convection regime are the overall (average) melting rate and the overall heat transfer rate passing through the heated wall. The average melting rate, $\bar{u}_0$, is obtained by combining Equation 24 with the definition

$$\bar{u}_0=\frac{1}{H}\int_0^H u_0\,\mathrm{d}y \tag{25}$$

This operation yields

$$\bar{u}_0=\frac{k\,\Delta T}{\rho h_{sf}H}\,\mathrm{Ra}^{1/4}\,\Phi \tag{26}$$

where the function Φ depends only on the Stefan number,

$$\Phi(\mathrm{Ste})=2\int_0^1\frac{\tau}{\tilde{\delta}}\,\mathrm{d}\tilde{y} \tag{27}$$

Figure 5 shows that Φ decreases significantly as Ste increases. In conclusion, relative to the melting rate that prevails in the limit of vanishing Stefan number [where $\Phi(0)=0.374$], the average melting rate in the quasi-steady regime decreases as Ste increases.

The overall heat transfer rate through the right wall is

$$Q_r=\int_0^H k\left(\frac{\partial T_r}{\partial x_r}\right)_0\mathrm{d}y \tag{28}$$

or, in terms of the overall Nusselt number for the right side

$$\mathrm{Nu}_r=\frac{Q_r}{k\,\Delta T}=\mathrm{Ra}^{1/4}\Phi_r(\mathrm{Ste}) \tag{29}$$

The function $\Phi_r(\mathrm{Ste})$ is shorthand for the integral

$$\Phi_r(\mathrm{Ste})=2\int_0^1\frac{1-\tau}{\tilde{\lambda}}\,\mathrm{d}\tilde{y} \tag{30}$$

which increases gradually as the Stefan number increases (Figure 5). In the Ste$=0$ limit the value of this integral approaches $\Phi_r(0)=0.374$, therefore the overall Nusselt number approaches $\mathrm{Nu}_r=0.374\,\mathrm{Ra}^{1/4}$. This zero-Ste estimate agrees well with the correlation $\mathrm{Nu}_r\cong 0.35\,\mathrm{Ra}^{1/4}$, which was obtained in Ref. 2 based on numerical simulations of the quasi-steady regime at Rayleigh numbers (Ra) as high as 10^8. The fact that the theoretical Nu_r is greater than the value provided by the numerical correlation is explained by the erosion of the upper portion of the two-phase interface in numerical and laboratory experiments. In the present analysis, the interface was treated as being nearly vertical all the way to the top of the enclosure, that is, all the way into the region that theoretically houses the highest heat flux and melting rate. In an actual experiment the high heat flux and melting rate of the upper region are moderated somewhat by the accentuated erosion and tilting of the interface.

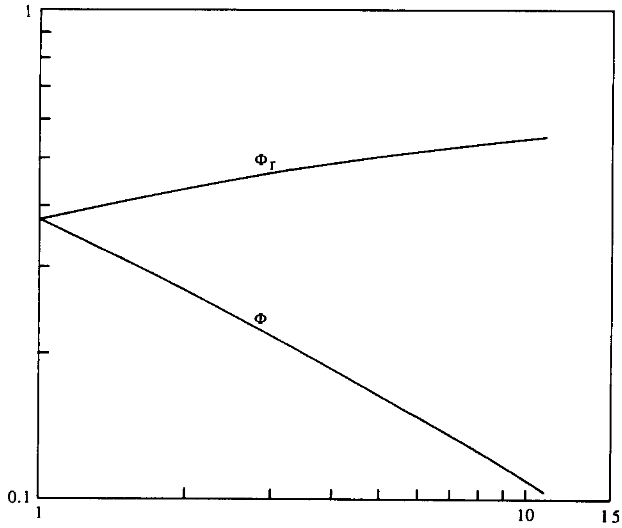

Figure 5 **The effect of Stefan number on the average melting rate (Φ) and the overall Nusselt number for heating from the side (Φ_r)**

A final observation concerns the widening gap between the Φ and Φ_r curves of Figure 5. To understand the physical meaning of this trend, consider the fact that the overall Nusselt number for heat transfer (Q) from the liquid to the interface is proportional to Φ,

$$\mathrm{Nu}=\frac{Q}{k\,\Delta T}=\bar{u}_0\,\frac{\rho h_{sf}H}{k\,\Delta T}=\mathrm{Ra}^{1/4}\Phi \tag{31}$$

In light of Equation 31, the gap between the Φ and Φ_r curves represents the difference between the heat transfer administered to the enclosure (Q_r) and the heat transfer absorbed at the interface (Q). The difference between the two heat transfer rates is set aside for the task of steadily warming up the newly generated liquid, that is, for the sensible heating of the new liquid so that its temperature rises to the "average" temperature of the liquid region.

Vertical counterflow in the conduction regime

The preceding solution documents only the quasi-steady regime, that is, the long-time behavior of the heat transfer and melting processes, when the heat transfer resistance across the liquid space is dominated by the two vertical boundary layers. It is possible, however, to continue this line of inquiry by focusing on the earlier stages of the phenomenon. In what follows, we see that the sizeable Stefan number effect that is felt in the quasi-steady regime is only the last vestige of an effect that is felt throughout the time-dependent regimes that precede the quasi-steady regime.

The earliest heat transfer regime is the one that is dominated by conduction. In this regime the thickness of the liquid gap is nearly constant. The temperature distribution across the gap is well known[9]

$$T=\Delta T\left[1-\frac{1}{\operatorname{erf}\Lambda}\operatorname{erf}\frac{x_1}{2(\alpha t)^{1/2}}\right] \tag{32}$$

where x_1 is measured in the direction shown in Figure 6. The parameter Λ is solely a function of the liquid-phase Stefan number,

$$\frac{\exp(-\Lambda^2)}{\operatorname{erf}\Lambda}=\pi^{1/2}\,\frac{\Lambda}{\mathrm{Ste}} \tag{33}$$

One noteworthy limit of this implicit relation is that of vanishingly small Stefan number,

$$\Lambda\rightarrow(\tfrac{1}{2}\mathrm{Ste})^{1/2}\qquad\text{as Ste}\rightarrow 0 \tag{34}$$

The liquid gap extends from $x_1=0$ to $x_1=X$, while the gap

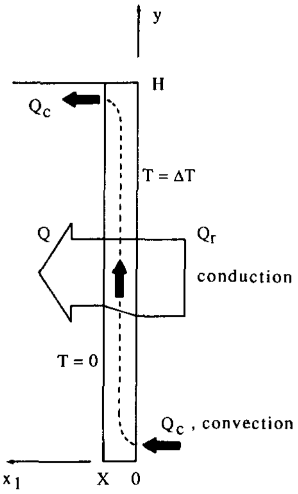

Figure 6 The coexistence of conduction and convection heat transfer during the time-dependent regime

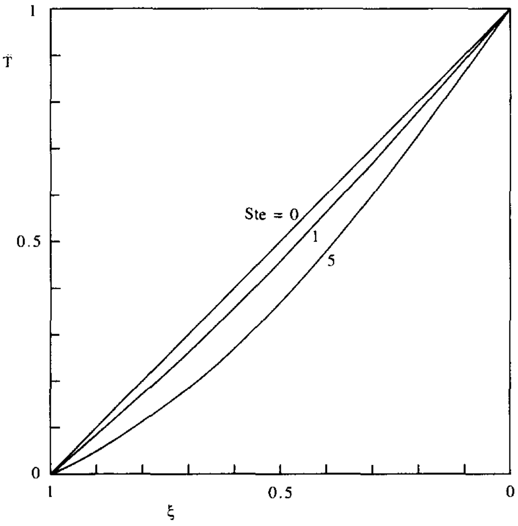

Figure 7 The effect of Stefan number on the temperature distribution across the slender liquid gap

thickness X is a function of both time and Stefan number,

$$X = 2\Lambda(\alpha t)^{1/2} \tag{35}$$

The distribution of temperature across the liquid gap is illustrated in Figure 7, where $\tilde{T}$ and ξ are the dimensionless temperature and horizontal position,

$$\tilde{T} = \frac{T}{\Delta T} \qquad \xi = \frac{x_1}{X} \tag{36}$$

The temperature profile is linear ($\tilde{T} = 1 - \xi$) in the Ste → 0 limit. The temperature gradient at the solid–liquid interface decreases as Ste increases. The opposite behavior is exhibited by the temperature gradient near the heated wall.

Less known than the temperature distribution is the fact that even when the liquid gap is extremely slender, the liquid is destined to circulate as a vertical counterflow.[10] In other words, the liquid is never stationary. Natural convection is present as soon as a *finite* ΔT is maintained across the vertical liquid gap, regardless of the actual size of ΔT. This feature distinguishes the vertical liquid layer geometry from the horizontal layer heated from below (Bénard convection), in which the transversal temperature difference must exceed a critical value before fluid motion can be observed.

With reference to the system of coordinates x_1-y of Figure 6, the momentum equation that governs the flow sufficiently far from the top and bottom ends of the liquid gap is the same as Equation 1, in which x is replaced by x_1. This equation can be integrated once to read

$$\frac{\partial^2 \tilde{v}}{d\xi^2} = \frac{\operatorname{erf}(\xi\Lambda)}{\operatorname{erf}(\Lambda)} + C_1 \tag{37}$$

in which the dimensionless velocity $\tilde{v}$ is defined as follows,

$$\tilde{v} = \frac{v}{g\beta\,\Delta T X^2/\nu} \tag{38}$$

Integrating Equation 37 twice more and using the no-slip boundary conditions $\tilde{v} = 0$ at $x = 0$ and $x = X$, we obtain

$$\tilde{v} = \tfrac{1}{2}C_1\xi(\xi - 1) + B(\xi) - \xi B(1) \tag{39}$$

In this expression the function $B(\xi)$ is shorthand for the integral

$$B(\xi) = \int_0^{\xi}\left[\int_0^{m} \frac{\operatorname{erf}(n\Lambda)}{\operatorname{erf}\Lambda}\,dn\right]dm \tag{40}$$

The remaining constant, C_1, is determined from the condition that at any instant in time the net vertical flow through the liquid gap is zero,

$$\int_0^1 \tilde{v}\,d\xi = 0 \tag{41}$$

In the end, the vertical velocity profile of Equation 39 assumes the form

$$\tilde{v} = \left[6\int_0^1 B(\xi)\,d\xi - 3B(1)\right]\xi(\xi - 1) + B(\xi) - \xi B(1) \tag{42}$$

This velocity distribution depends not only on ξ but also on Λ, because Λ appears in the integrand of the B integral, Equation 40. This feature is illustrated by Figure 8, which shows further that the plane of flow reversal ($\tilde{v} = 0$) migrates away from the solid–liquid interface as the Stefan number increases. In the Ste → 0 limit, the $\tilde{v}$ profile becomes centrosymmetric about the midplane $\xi = \frac{1}{2}$,

$$\tilde{v} = \tfrac{1}{12}\xi(1 - \xi)(1 - 2\xi) \tag{43}$$

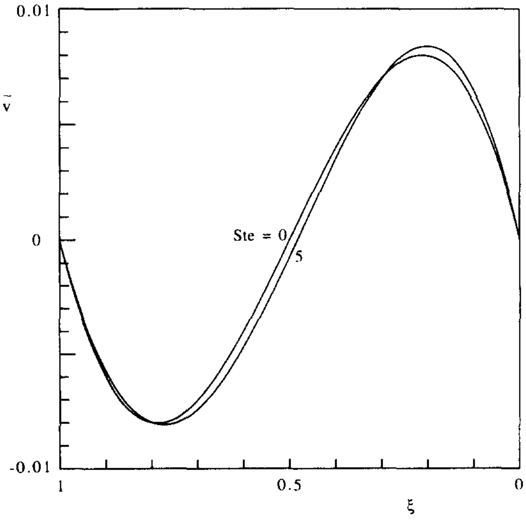

Figure 8 The effect of Stefan number on the vertical velocity distribution across the slender liquid gap

In this limit the vertical velocity profile is the same as that of a fluid held in the gap between two tall vertical plates at different temperatures.[10]

Time-dependent heat transfer and melting rates

The new heat transfer-type feature of the slender-gap limit discussed above is that the counterflow of Figure 8 convects heat at a finite rate in the vertical direction. The convection heat transfer rate (Q_c) originates from the lower extremity of the heated wall, and is absorbed by the top end of the solid–liquid interface (Figure 6). The presence of this convection contribution is another example of a general feature of all counterflow heat exchangers: any such heat exchanger convects heat in the longitudinal direction, when a net difference exists between the bulk temperatures of its two branches.

The convection heat transfer rate can be calculated by performing the integral

$$Q_c = \int_0^X \rho v c T \, dx \qquad (44)$$

which, in dimensionless terms, reads

$$\frac{Q_c}{k \Delta T} = \mathrm{Ra}\, \theta^{3/2} G_c \qquad (45)$$

In this expression, θ is the dimensionless time

$$\theta = \frac{\alpha t}{H^2} \mathrm{Ste} \qquad (46)$$

and G_c is a function of only the Stefan number,

$$G_c(\mathrm{Ste}) = (2\Lambda\, \mathrm{Ste}^{-1/2})^3 \int_0^1 \tilde{v}\tilde{T} \, d\xi \qquad (47)$$

In the Ste → 0 limit, for example, the definite integral appearing in Equation 47 equals 1/720, and, via Equation 34, the function G_c equals $2^{1/2}/360$. This and other representative values of the function G_c have been plotted in Figure 9. The numerical error in the calculated G_c values is less than 1%.

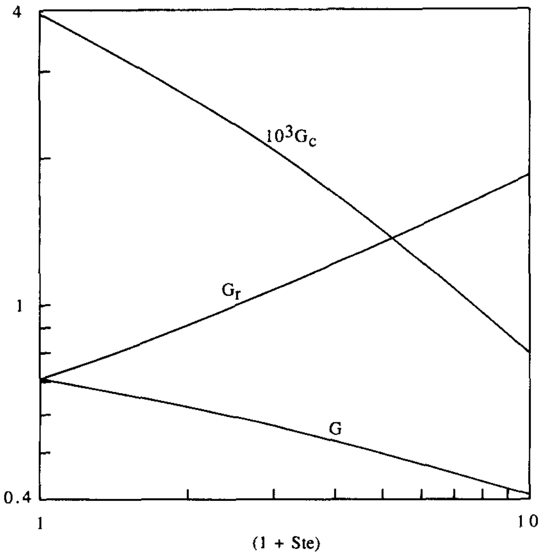

Figure 9 The functions G_c, G_r, and G that govern the overall heat transfer and average melting rates in the time-dependent regime

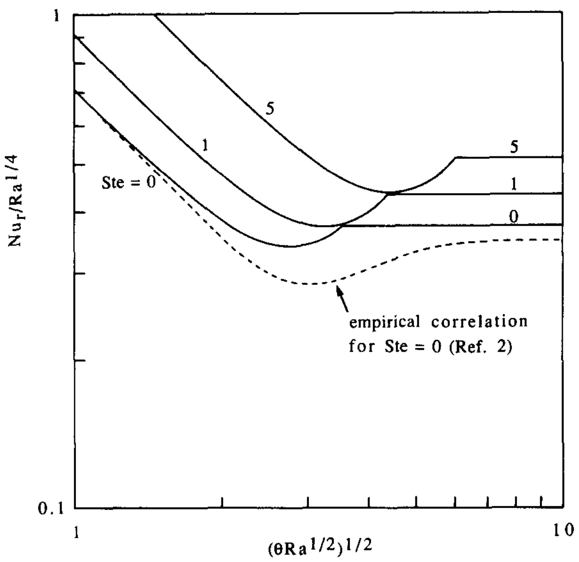

Figure 10 The effect of Stefan number on the history of the overall heat transfer rate

The total heat transfer rate administered to the heated wall of the enclosure (Q_r) can be calculated by adding the convection contribution Q_c to the thermal diffusion heat transfer collected over the $x_1 = 0$ wall

$$Q_r = -kH\left(\frac{\partial T}{\partial x_1}\right)_{x_1=0} + Q_c \qquad (48)$$

The additive form of the right side of Equation 48 is suggested by the geometry of Figure 6, that is, by the fact that the "wide" thermal diffusion current is perpendicular to Q_c. When the liquid gap is extremely slender ($X \ll H$), the thickness X is independent of y over most of the height H. As a consequence, the thermal diffusion current is unaware of the presence of Q_c, which proceeds vertically and erodes only the uppermost end of the solid–liquid interface.

Applying one more time the Nu_r definition given in the first part of Equation 29, the nondimensional version of Equation 48 becomes

$$\mathrm{Nu}_r = G_r \theta^{-1/2} + \mathrm{Ra}\, \theta^{3/2} G_c \qquad (49)$$

where G_r is also a function of only the Stefan number (Figure 9),

$$G_r = \frac{\mathrm{Ste}^{1/2}}{\pi^{1/2} \operatorname{erf} \Lambda} \qquad (50)$$

The surface $\mathrm{Nu}_r(\mathrm{Ra}, \theta, \mathrm{Ste})$ can be "condensed" in two dimensions by plotting the ratio $\mathrm{Nu}_r/\mathrm{Ra}^{1/4}$ versus $(\theta\, \mathrm{Ra}^{1/2})$, as done in Figure 10. Equation 49 becomes

$$\frac{\mathrm{Nu}_r}{\mathrm{Ra}^{1/4}} = G_r(\theta\, \mathrm{Ra}^{1/2})^{-1/2} + G_c(\theta\, \mathrm{Ra}^{1/2})^{3/2} \qquad (51)$$

This form and Figure 10 show that the right-side Nusselt number reaches a minimum when the abscissa group is of order one. The minimum migrates slowly toward higher values of $(\theta\, \mathrm{Ra}^{1/2})$ as Ste increases. Each constant-Ste curve in Figure 10 is terminated at the point where the $\mathrm{Nu}_r/\mathrm{Ra}^{1/4}$ ratio reaches the plateau indicated by the quasi-steady heat transfer solution of Equation 29.

The piecewise-continuous curve formed by joining Equation 29 and Equation 51 moves toward higher $(\mathrm{Nu}_r/\mathrm{Ra}^{1/4})$ and $(\theta\, \mathrm{Ra}^{1/2})$ values as Ste increases. During this shift the curve retains its shape, namely, the nearly straight negative-slope portion that indicates the conduction dominated regime, the minimum associated with the competition between conduction and convection, and, finally, the plateau of the quasi-steady regime. This sequence of bends in the curve can be anticipated also based on scale analysis.[2] The contribution of the present work is that it pinpoints the shape and location of the Nu_r curve without relying on any empirical constants.

The dashed-line in Figure 10 is the three-constant empirical (numerical) correlation developed in Ref. 2 based on scale analysis and numerical experiments at Rayleigh numbers as high as 10^8. The minimum of the theoretical curve occurs almost at the same time ($\theta\,\mathrm{Ra}^{1/2}$) as the minimum of the empirical correlation. The theory generally overestimates the numerical calculations, the largest difference being of the order of 19% in the region of the Nu_r minimum. The discrepancy between theory and numerical experiments improves (decreases) to 7% in the long-time, quasi-steady regime.

The average melting rate during the time-dependent regime can be estimated using the $\bar{u}_0$ value listed in Equation 31,

$$\bar{u}_0 = \frac{k\,\Delta T}{\rho h_{sf} H}\,\mathrm{Nu} \tag{52}$$

in which $\mathrm{Nu} = Q/(k\,\Delta T)$, and where Q is the total heat transfer rate absorbed by the solid–liquid interface,

$$Q = -kH\left(\frac{\partial T}{\partial x_1}\right)_{x_1 = X} + Q_c \tag{53}$$

Dividing this by $k\,\Delta T$ we obtain the overall Nusselt number for the cold side,

$$\mathrm{Nu} = G\theta^{-1/2} + \mathrm{Ra}\,\theta^{3/2} G_c \tag{54}$$

where G is a new function of Ste,

$$G(\mathrm{Ste}) = \frac{\mathrm{Ste}^{1/2}}{\pi^{1/2}\,\mathrm{erf}\,\Lambda}\exp(-\Lambda^2) \tag{55}$$

In combination with Equation 52, the cold-side Nusselt number of Equation 54 delivers the desired melting rate.

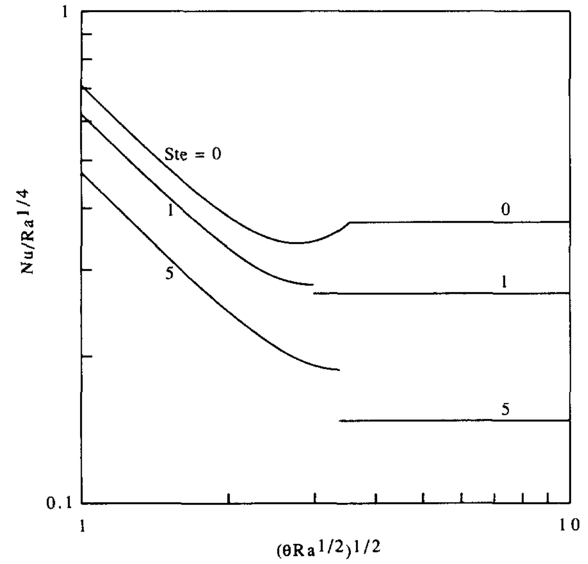

Figure 11 The effect of Stefan number on the history of the average melting rate

The $\mathrm{Nu}(\mathrm{Ra}, \theta, \mathrm{Ste})$ surface (54) too can be cast in two dimensions by dividing by $\mathrm{Ra}^{1/4}$ and plotting the resulting constant–Ste curves in Figure 11,

$$\frac{\mathrm{Nu}}{\mathrm{Ra}^{1/4}} = G(\theta\,\mathrm{Ra}^{1/2})^{-1/2} + G_c(\theta\,\mathrm{Ra}^{1/2})^{3/2} \tag{56}$$

Shown on the same graph are the plateau $\mathrm{Nu}/\mathrm{Ra}^{1/4}$ values found for the quasi-steady regime, that is, the value of $\Phi(\mathrm{Ste})$ of Equations 31 and 27. We see that as Ste increases above 1 the time-dependent function (56) fails to intersect the horizontal line that accounts for the quasi-steady regime. This behavior suggests that the true (smooth) Nu curve loses its characteristic minimum above a certain Stefan number of order 1. This conclusion is markedly different than the one drawn from Figure 10, in which the characteristic shape of the Nu_r curve appears to be preserved regardless of Stefan number.

Conclusion

The primary objective of this paper was to demonstrate that it is possible to anticipate theoretically the main features of the time-dependent and quasi-steady regimes of melting with natural convection in an enclosure heated from the side. The present work describes the manner in which the liquid superheat (Ste) influences the overall heat transfer and melting rates.

Acknowledgment

This work was supported by the Electric Power Research Institute contract no. RP 8006-4, under the management of Dr. Jong H. Kim.

References

1 Viskanta, R. Natural convection melting and solidification, in *Natural Convection: Fundamentals and Applications*, ed. by S. Kakac, W. Aung, and R. Viskanta, Hemisphere, Washington, DC, 1985, 845–877

2 Jany, P. and Bejan, A. Scaling theory of melting with natural convection in an enclosure. *Int. J. Heat Mass Transfer* 1988, **31**, 1221–1235

3 Gill, A. E. The boundary layer regime for convection in a rectangular cavity. *J. Fluid Mechanics* 1966, **26**, 515–536

4 Bejan, A. *Convection Heat Transfer*, Wiley, New York, 1984

5 Kuiken, H. K. Boundary layer conditions in free convection. *J. Eng. Math.* 1968, **2**, 95–105

6 Patterson, J. and Imberger, J. Unsteady natural convection in a rectangular cavity. *J. Fluid Mechanics* 1980, **100**, 65–86

7 Blythe, P. A. and Simpkins, P. G. Thermal convection in a rectangular cavity. *Physicochemical Hydrodynamics* 1977, **2**, 511-524

8 Squire, H. B. Integral solution published in *Modern Developments in Fluid Dynamics, II* ed. by S. Goldstein, Dover, New York, 1965, 641–643

9 Carslaw, H. S. and Jaeger, J. C. *Conduction of Heat in Solids*, 2nd ed. Oxford University Press, Oxford, 1959, 287

10 Rohsenow, W. M. and Choi, H. Y. *Heat, Mass and Momentum Transfer*. Prentice-Hall, Englewood Cliffs, New Jersey, 1961, 142–146